A hybrid compressible-incompressible CFD method for Richtmyer-Meshkov mixing

Tommaso Oggian
Cranfield University
Cranfield
MK43 0AL
United Kingdom

Dimitris Drikakis *
Cranfield University
Cranfield
MK43 0AL
United Kingdom
Email: d.drikakis@cranfield.ac.uk

David L. Youngs
Robin R.J.R. Williams
AWE
Aldermaston
RG7 4PR
United Kingdom

ABSTRACT

This paper presents a hybrid compressible-incompressible approach for simulating the Richtmyer-Meshkov instability (RMI) and associated mixing. The proposed numerical approach aims to circumvent the numerical deficiencies of compressible methods at low Mach numbers, when the flow has become essentially incompressible. A compressible flow solver is used at the initial stage of the interaction of the shock wave with the fluids interface and the development of the Richtmyer-Meshkov instability. When the flow becomes sufficiently incompressible, based on a Mach number prescribed threshold, the simulation is carried out using an incompressible flow solver. Both the compressible and incompressible solvers use Godunov-type methods and high-resolution numerical reconstruction schemes for computing the fluxes at the cell interfaces. The accuracy of the model is assessed by using results for a 2D single-mode RMI.

*Address all correspondence related to ASME style format and figures to this author.

1 Introduction

A number of studies have shown that Godunov-type methods for compressible flows become very dissipative when the Mach number is sufficiently low [1–7]. A first analysis of the problem was presented by [2,8,9], and more recently by [5,6]. A review of different approaches regarding the above problem can be found in [7]. In brief, a statement of the problem has as follows. The solution of the compressible Euler equations, $s(\mathbf{x},y)$, can be split into a fast acoustic component $s_{\text{fast}}(\mathbf{x},t,t/M^*)$, where M^* is the reference Mach number, and a slow component, $s(\mathbf{x},t) = s_{\text{fast}}(\mathbf{x},t,t/M^*) + s_{\text{slow}}(\mathbf{x},t) + O(M^*)$, where s_{slow} ($O(M^2)$) represents the solution of the incompressible system. Carrying out the asymptotic analysis for the discrete Euler equations and comparing the results with the exact solution, it was shown [3,4] that the solution of the Riemann problem at the cell interface creates an artificial acoustic wave of the same order of magnitude ($O(M^*)$), which destroys the incompressible sought solution. This is known in the literature as "cancellation error" (see [5] and references therein). Further analysis by [5] linked the entropy generation with the dissipation of kinetic energy in Godunov-type schemes, proving that the projection of the initial data on piecewise constants creates an artificially velocity jump at the cell interface.

In addition to the cancellation error, compressible simulations based on explicit numerical schemes encompass numerical efficiency issues due to time step restrictions. The time-step is commonly dictated by the highest eigenvalue of the system $\Delta t = C\Delta x/\lambda^n$, where C is the CFL number, $\lambda^n = \max\{|u_q| + a_q\}$, and the subscript $(.)_q$ denotes the three directions x,y and z. When the Mach number of the flow is low and the sound speed a_q becomes significantly larger than the speed with which the flow evolves (u_q), the speed of acoustic waves determines the time step value, thus resulting in a clear loss of time-marching efficiency. In order to overcome the above numerical problem, three main research directions have been pursued so far. The first approach concerns modification of the numerics for solving the compressible Euler equations, by introducing either a reference state for the variables and performing the calculations only with respect to their fluctuations [10], or a predictor-corrector type algorithm that involves the solution of one [11,12], or two elliptic-equations for the pressure [13]. The second approach, adopted by [3] and by [14], concerns the modification of the Riemann-solver by either compensating for, or modifying, the strength of the acoustic waves. The third approach [6] corrects the extrapolated quantities locally on the mesh in order to reduce the artificial velocity jump at the cell interfaces. Although the aforementioned approaches offer a partial remedy to the problem, accuracy and efficiency issues regarding the use of compressible solvers at (very) low Mach numbers, when the flow becomes essentially incompressible, still remain unresolved.

In the present paper, we propose a hybrid compressible-incompressible approach which is suitable for multi-mode RMI mixing. In order to assess accuracy, the method is tested on a 2D single-mode RMI problem and its results are compared against compressible solutions. Although the present study is motivated by accuracy issues at late time RMI mixing, the use of the hybrid compressible-incompressible approach is relevant to every fluid mechanics problem that features compressibility ar early times and incompressible flow behaviour at later times such as combustion applications and astrophysics.

2 Numerical model

The compressible model is based on the Euler equations in a conservative form

$$\frac{\partial \mathbf{U}}{\partial t} + \frac{\partial \mathbf{E}}{\partial x} + \frac{\partial \mathbf{F}}{\partial y} = 0 \ , \tag{1}$$

where

$$\begin{cases} \mathbf{U} = (\rho, \rho u, \rho v, E)^{\mathrm{T}} \\ \mathbf{E} = (\rho u, \rho u^2 + p, \rho uv, (E+p)u)^{\mathrm{T}} \\ \mathbf{F} = (\rho v, \rho uv, \rho v^2 + p, (E+p)v)^{\mathrm{T}} \end{cases} . \tag{2}$$

and ρ is the density of the fluid, u and v are the Cartesian components, p is the pressure, e is the internal energy and $E = \rho e + 0.5\rho(u^2 + v^2)$ is the total energy per unit volume. The system is closed by the equation of state for ideal gases $p = \rho e(\gamma - 1)$, where γ is the ratio of specific heats. The convective fluxes are computed by solving the Riemann-problem at the cell interfaces using the characteristics-based solver [15–17]:

$$\mathbf{E}^{\mathrm{CB}}_{i+\frac{1}{2}} = \begin{pmatrix} \widetilde{\rho u} \\ \widetilde{\rho u}^2/\tilde{\rho} + \tilde{p} \\ \widetilde{\rho u}\widetilde{\rho v}/\tilde{\rho} \\ \widetilde{\rho u}\widetilde{\rho w}/\tilde{\rho} \\ \widetilde{\rho u}(\tilde{E} + \tilde{p})/\tilde{\rho} \end{pmatrix} . \tag{3}$$

The flow variables at the cell interfaces are given by

$$\widetilde{\rho} = \rho_0 + r_1 + r_2 \ , \tag{4}$$

$$\widetilde{\rho u} = (\rho u)_0 + (u+c)r_1 + (u-c)r_2 \ , \tag{5}$$

$$\widetilde{\rho v} = (\rho v)_0 + (v+c)r_1 + (v-c)r_2 \ , \tag{6}$$

$$\widetilde{\rho w} = (\rho w)_0 + (w+c)r_1 + (w-c)r_2 \ , \tag{7}$$

$$\widetilde{E} = E_0 + (H + a\lambda_0)r_1 + (H - a\lambda_0)r_2 \ . \tag{8}$$

Here, H is the total enthalpy, c is the speed of sound and the terms r_1 and r_2 are defined by

$$r_1 = \frac{1}{2\gamma}(q_1 - q_0) \ , \tag{9}$$

$$r_2 = \frac{1}{2\gamma}(q_2 - q_0) \ , \tag{10}$$

where q_n, with $n = 1,2,3$, are the variables along the three characteristics:

$$q_n = \frac{1}{2}([1 + \text{sign}(\lambda_n)]U_L + [1 - \text{sign}(\lambda_n)]U_R) \ , \tag{11}$$

and λ_n, $n = 0,1,2$ are the system eigenvalues. The variables at the left and right of the cell interface $\mathbf{U}_L$ and $\mathbf{U}_R$ are calculated using the TVD-MUSCL scheme:

$$\begin{aligned} \mathbf{U}_L &= \mathbf{U}_i + \frac{1}{2}\varphi(r_L)(\mathbf{U}_i - \mathbf{U}_{i-1}) \ , \\ \mathbf{U}_R &= \mathbf{U}_i + \frac{1}{2}\varphi(r_R)(\mathbf{U}_{i+2} - \mathbf{U}_{i+1}) \ , \end{aligned} \tag{12}$$

where:

$$\begin{aligned} r_L &= \frac{\mathbf{U}_{i+1} - \mathbf{U}_i}{\mathbf{U}_i - \mathbf{U}_{i-1}} \ , \\ r_R &= \frac{\mathbf{U}_i - \mathbf{U}_{i-1}}{\mathbf{U}_{i+1} - \mathbf{U}_i} \ , \end{aligned} \tag{13}$$

The limiter $\varphi(r_K)$ $(K = R,L)$ is defined by [18]:

$$\begin{aligned} \varphi(r_L) &= \max[0, \min(2, 2r_L, \beta_L)] \ , \\ \varphi(r_R) &= \max[0, \min(2, 2r_{R+1}, \beta_R)] \ . \end{aligned} \tag{14}$$

where

$$\begin{aligned}\beta_L &= \frac{-2/r_{L,i-1}+11+24r_{L,i}-3r_{L,i}r_{L,i+1}}{30}\,,\\ \beta_R &= \frac{-2/r_{R,i+2}+11+24r_{R,i+1}-3r_{R,i+1}r_{R,i}}{30}\,.\end{aligned} \tag{15}$$

The above formulas allow up to fifth-order of accuracy. To reduce the numerical dissipation at low Mach numbers, the modifications proposed in [6], henceforth labelled as "Low-Mach correction" (LM), were also implemented.

The incompressible model is based on the Euler equations for variable density flow

$$\begin{cases}\dfrac{\partial u}{\partial x}+\dfrac{\partial v}{\partial y}=0\\[2ex] \dfrac{\partial(\rho\mathbf{U}_\mathrm{I})}{\partial t}+\dfrac{\partial(\rho\mathbf{E}_\mathrm{I})}{\partial x}+\dfrac{\partial(\rho\mathbf{F}_\mathrm{I})}{\partial y}=-\nabla p\end{cases}, \tag{16}$$

$$\begin{cases}\mathbf{U}_\mathrm{I}=(u,v,1)^\mathrm{T}\\ \mathbf{E}_\mathrm{I}=(u^2,uv,u)^\mathrm{T}\\ \mathbf{F}_\mathrm{I}=(uv,v^2,v)^\mathrm{T}\end{cases}. \tag{17}$$

A review of methods for incompressible flows can be found in [7]. The variable density, 'incompressible' equations, are also solved in conservative form due to the coupling with the density transport equation. The incompressible fluxes are computed by the Riemann-solver of [19]:

$$\mathbf{E}^{\mathrm{RU}}_{i+\frac{1}{2}}=\frac{1}{2}\left[(\mathbf{E}_L+\mathbf{E}_R)-S(\mathbf{U}_R-\mathbf{U}_L)\right], \tag{18}$$

where S is the highest wave speed computed in the cell:

$$S=\max\{|u_L-a_L|,|u_R-a_R|,|u_L+a_L|,|u_R+a_R|\}\,. \tag{19}$$

Since in the incompressible fluid model the information travels across the domain with infinite speed, it is not possible to directly apply (19) and a new definition for S is required. The real wave speed of the compressible model is therefore replaced by a 'fictitious' wave speed, which assumes that the information travels across the cell with the speed of the fluid. Therefore, the new $\overline{S}$ simply becomes:

$$\overline{S} = \max\{|u_L|, |u_R|\} \ . \tag{20}$$

In the present paper, the Pressure-Projection (PP) technique [20, 21] has been employed to solve the system (16). PP makes use of the Hodge decomposition [22] of the velocity field into parts that are divergence and curl-free: $\widetilde{\mathbf{U}} = \mathbf{U}_{\mathrm{I}} + \nabla\phi$, where $\mathbf{U}_{\mathrm{I}}$ is the divergence-free component of the solution $\widetilde{\mathbf{U}}$. The gradient $\nabla\phi$ of the potential ϕ denotes the curl-free portion. Taking the divergence of the above equation gives $\nabla \cdot \widetilde{\mathbf{U}} = \nabla^2\phi$. Once ϕ has been computed, then the solution can be found through $\mathbf{U}_{\mathrm{I}} = \widetilde{\mathbf{U}} - \nabla\phi$. The problem is therefore split into a hyperbolic equation for the momentum and an elliptic equation for the pressure:

$$\nabla \cdot \left(\frac{1}{\rho} \nabla p \right) = \frac{1}{\Delta t} \nabla \cdot \widetilde{\mathbf{U}} \ . \tag{21}$$

Once p is computed, it is used to recover the divergence-free component of $\widetilde{\rho\mathbf{U}}$: $\rho\mathbf{U}_{\mathrm{I}} = \widetilde{\rho\mathbf{U}} - \nabla p$. The solution is obtained in three steps:

1. The momentum equation in (16) is advanced in time without the pressure term:

$$\left(\widetilde{\rho\mathbf{U}}\right)^{n+1} = (\rho\mathbf{U})^n + \Delta t \left[- \left(\frac{\partial(\rho\mathbf{E})}{\partial x} + \frac{\partial(\rho\mathbf{F})}{\partial y} \right) \right] \ . \tag{22}$$

2. The linear system of equations arising from the numerical discretisation of the Poisson equation (21) is solved by the Stabilised Bi-Conjugate Gradients (Bi-CGSTAB) method [23]. Due to the nature of the methods used in this study as well as the data structure of the computer code, a collocated grid arrangement for the unknown variables was employed, ie, the flow variables are stored in the cell centres.
3. The tilde-solution from (22) is projected onto the divergence-free space and the final incompressible solution is recovered:

$$(\rho\mathbf{U})^{n+1} = \widetilde{(\rho\mathbf{U})}^{n+1} - \Delta t \nabla p^{n+1}. \tag{23}$$

The multi-component model comprises $N-1$ (N is number of species) advective equations for passive scalars, φ_i ($1 \leq i \leq N$) which are solved together with the Euler equations:

$$\frac{\partial \varphi_i}{\partial t} + \frac{\partial (u\varphi_i)}{\partial x} + \frac{\partial (v\varphi_i)}{\partial y} = 0 \ . \tag{24}$$

These equations cast in different terms, e.g., density, mass fraction, volume fraction, depending on the nature of the problem. In the present RMI simulations, two fluids have been considered, hence one advection equation has been added to the Euler equations. In the compressible part of the simulation, if γ and C_v (specific heat at constant volume) are the same for both fluids considered here (thus the simulation results do not depend on their values), the additional transport equation casts in terms of the density multiplied by volume fraction, $\varphi = \rho V_f$. In the incompressible part of the simulation, the transport equation is casted in terms of total density.

The numerical transition (henceforth labelled as 'NT') from the compressible to the incompressible solver is based on the local Mach number of the flow, M which is calculated at each time step of the compressible solver. NT is activated when M is less than a given threshold M_{NT}. For RMI simulations, it was found that $M_{\mathrm{NT}} = 0.2 - 0.3$ gives satisfactory results (see further discussion in Section 3). The pressure is initialised by the Poisson solver during the first time step. For the first guess for the iteration procedure, the pressure is calculated by the total energy equation but use of a constant pressure throughout the domain also gives satisfactory convergence. At the beginning of the incompressible simulation, the density is calculated using the volume fraction available from the compressible solution: $(\rho_{\mathrm{MIX}})_{\mathrm{I}} = V_f(\rho_1)_{\mathrm{I}} + (1 - V_f)(\rho_2)_{\mathrm{I}}$. The incompressible densities, ρ_1 and ρ_2 are calculated by averaging the densities in the cells with $V_f = 0$ and $V_f = 1$ at the end of the compressible simulation. The density is subsequently updated at each time step through the solution of (16). A third-order accurate Runge-Kutta time-stepping method was used for both compressible and incompressible simulations.

3 Numerical tests

To investigate the accuracy of the hybrid compressible-incompressible method for RMI problems, a 2D single-mode RMI case has been considered. The dimensions of the computational domain are: $-4\pi < x < 4\pi$ (this does not include the extended 1D domain used for boundary condition purposes; see discussion below), $0 < y < 2\pi$ and the initial conditions, as per [24], consist of a light and a heavy gas separated by a sinusoidal perturbation of amplitude 0.2 and an incident shock-wave of Mach number 1.5 travelling from the light ($\rho = 1.15 kg/m^3$) to the heavy ($\rho = 5.77 kg/m^3$) fluid along the

x-direction. In the hybrid solution, the time step at the end of the compressible stage was $\Delta t \approx 2.2 \times 10^{-5}$ s using a CFL=0.5. In order to preserve Δt at the first incompressible time-step, the CFL for the incompressible solver was set as 0.04. At the very end of the simulation ($t = 0.2$s), the compressible time-step remained around 2.2×10^{-5} s, whereas the incompressible solver uses $\Delta t \approx 4.5 \times 10^{-5}$ s. This clearly highlights the gain in time-stepping efficiency, which is achieved by using the incompressible solver at late times, thus making the hybrid solver more efficient than the fully compressible one for very-long time simulations. The hybrid solver is approximately 2.5 faster than the full compressible method for long time simulations. The comparison between the compressible and hybrid solvers is based on total wall clock time required to run the flow case on the same computer (using the same number of processors). Note that the CFL number in the incompressible simulation could gradually increase its value, thus improving further the efficiency of the simulations. However, the value of CFL is also dictated by accuracy issues. A larger CFL value would result in larger time steps, which can compromise the accuracy of the simulation. In this study we found that CFL=0.04 results in a good 'compromise' between accuracy and computational cost.

In the compressible stage of the computations, the boundary conditions are periodic in the direction normal to the shock propagation, whereas a one-dimensional extended domain (beyond the computational domain) is used at both the inlet and the outlet of the shock-tube in order to allow the shocks to exit the domain preventing their excessive reflection. The extended domain comprises 7000 cells with the same step size as the cells in the main domain. That's enough to prevent to the re-shock of the interface due to reflection at the end of the extended domain.This technique does not completely eliminate the reflection of the shock waves, which is impossible to cancel where the mesh size changes, but it reduces their magnitude by approximately 99.97% [25]. When switching to the incompressible scheme, the one-dimensional extended domain containing the shocks was disconnected from the main domain and was replaced by a symmetry boundary condition.

There is a limited number of previous RMI studies dealing with the transition of the flow from the compressible to the incompressible regime. Based on experimental evidence for a single mode RMI, [26] suggested that the transition time is $t \approx 1/k^2 A \Delta u a_0$ ($t = 0$ is considered to be the time instant where the shock reaches the initial interface), where k and a_0 are the wavenumber and initial amplitude of the perturbation. [27] also proposed a similar relation $t \approx 1/k^2 M_0 c_0 a_0$, where M_0 is the Mach number of the incident shock and c_0 is the speed of sound in the fluid ahead of it. For the present RMI case, the transition time according to Aleshin's et al. formula should be $t = 0.06513s$. However, our numerical test showed that the transition, based on the local Mach number threshold of 0.2, occurs at an earlier time t_{NT} $0.052s$, which coincides approximately with the time the shock wave leaves the domain. Several numerical tests aimed at addressing the sensitivity of the incompressible solver with respect to the transition Mach number were carried out. Using $M_{\mathrm{NT}} = 0.2$ and $M_{\mathrm{NT}} = 0.3$ showed to have no influence in the evolution of the instability; however, the number of iterations in the Poisson solver for reaching convergence slightly varied and the best 'compromise' in terms of efficiency was found to be achieved for $M_{\mathrm{NT}} = 0.3$. It was found that applying a residual threshold of $r = 1 \times 10^{-4}$ (dimensionless) in the solution of the pressure-Poisson equation gives satisfactory results. Grid convergence tests were performed using four uniform, block-structured, computational grids: 64×16 (G1), 128×32 (G2), 256×64 (G3) and 512×128 (G4). The growth of the mixing layer, W_s, was used for comparing the results on different grids. For the single-mode case W_s is defined by

$$W_s = \frac{h_b + h_s}{2} \ , \tag{25}$$

where h_b and h_s are the height of bubble (portion of light fluid penetrating the heavy fluid) and spike (portion of heavy fluid penetrating the light fluid), respectively. These quantities are computed at each time step as the distance between the initial position of the interface and the position where $V_f = 0.5$. The grid convergence results for the C, C+LM, and H methods are shown in Table 1. The grid converge index (GCI) [28] with respect to the growth of the mixing layer is defined as:

$$\mathrm{GCI} = F_s \frac{|\varepsilon|}{r^p - 1} \ . \tag{26}$$

where ε is the relative error between two successively refined grids and the constants have values: $F_s = 3$, $p = 2$ and $r = 2$, which means that for the chosen parameters GCI $= |\varepsilon|$ (the smaller the better). is. Full compressible simulations of the single-mode RMI case were performed to compare the results with the hybrid solver. The compressible simulations were carried out with the low-Mach correction (henceforth labelled as 'C+LM') and without the low-Mach correction (henceforth labelled as 'C'). The solutions obtained using the hybrid solver are labelled as 'H'. Fig. 1 and Table 1 show that convergence on G3 is achieved by the H method. However, good results are also achieved on G2 and an adequate approximation is obtained on G1. Overall, the H method performs better than C and C+LM method.

Time	C			C+LM			H		
[s]	G1-G2	G2-G3	G3-G4	G1-G2	G2-G3	G3-G4	G1-G2	G2-G3	G3-G4
0.10	5.02	2.24	1.32	5.10	1.41	1.15	4.55	1.16	0.42
0.15	1.34	1.17	1.33	2.68	2.96	1.04	3.69	0.46	0.34
0.20	4.51	2.43	2.11	1.31	4.67	1.37	2.83	1.02	0.38

Table 1. GCI [%] at different instants for the C, C+LM and H solvers.

The averaged $|\nabla \cdot \mathbf{U}|$ throughout the computational domain, for the C+LM and H methods, and for times $t > t_{NT}$ is shown Fig. 2. C+LM gives small values of $|\nabla \cdot \mathbf{U}|$ but still far from being considered divergence-free. For $t > 0.052$ s traces of compressibility still exist. The hybrid approach gives divergence-free velocity field with $|\nabla \cdot \mathbf{U}|$ being of the order of 10^{-2} s^{-1} decreasing to 10^{-3} s^{-1} for $t \geq 0.08$ s. In Fig. 3, the velocity divergence along the central line ($y = \pi$) is plotted for the C+LM and H solutions for times $t > t_{\mathrm{NT}}$. The C+LM results show an irregular spatial pattern of $\nabla \cdot \mathbf{U}$, which becomes smoother (and decreasing in value) at late times. The H solution gives $\nabla \cdot \mathbf{U} < 10^{-3}$.

Time [s]	$W_{s-\mathrm{C+LM}}$	$W_{s-\mathrm{H4}}$	$\varepsilon_r[\%]$
0.075	1.18	1.20	1.03
0.100	1.37	1.38	1.27
0.125	1.51	1.53	1.14
0.150	1.63	1.65	1.22
0.175	1.74	1.76	1.39
0.200	1.83	1.86	1.74

Table 2. Relative error between the C+LM and H solutions with reference to the compressible solution (see also Fig. 4).

A comparison of the growth of the mixing width for the C, C+LM and H methods on G2 and G4 is shown in Fig. 4. In both the grids, the lines start bifurcating after t_{NT}. The discrepancies between the three solution methods on G4 are small, whereas a they are clearly visible when looking at G2, especially at later times. Table 2 shows the relative error between the different solutions; the C+LM and H solutions are compared with the solution of the compressible solver (C) without low-Mach correction. The inset plot in Fig. 4b shows that the transition from the compressible to the incompressible solution takes place smoothly and that the low-Mach correction does not have any noticeable effects on the mixing width results when grid-convergence is achieved. This is further confirmed by Fig. 6, where it is possible to see some snapshots of the volume fraction field at different instants in time from the switching moment. On the other hand, in Fig. 4(a), where grid convergence is not yet achieved, it is possible to notice the difference in the predicted growth. Here, the mixing computed by the H solver lies in between the compressible methods. Contrarily from G4, the use of low-Mach correction on a coarse grid makes a noticeable difference with an increased predicted mixing (see also Fig. 5).

According to Figures 5 and 6, the C and C+LM mushroom predictions at resolution G2 are diffused and hazy with one roll-up, whereas the H results are less diffused (due to the incompressible solver), featuring two roll-ups. At resolution G4, the C+LM solution gives a less diffused mushroom and roll-ups compared to the C solution. The H solution gives an even sharper mushroom compared to C+LM. At late times the vortices in the C and C+LM solutions are rolled-up twice, whereas the H solution results in three roll-ups.

4 Concluding remarks

A hybrid compressible-incompressible method for RMI flows was presented. Numerical tests were carried out for a 2D, single-mode RMI case. The results from the hybrid method were compared with compressible solutions, including a variant of the compressible solver based on a low-Mach correction. The relative error in the results of the three different methods (H, C+LM and C) with respect to the growth of the mixing width was small. The transition from the compressible to the incompressible solution did not create any unphysical artifacts. The hybrid solver gave a sharper mushroom compared to C and C+LM and the two symmetric vortices had three roll-ups at late time compared to two roll-ups in the case of the C and C+LM methods at the finest resolution. It is expected that for multimode calculations sufficient accuracy should be obtained

with 16 meshes per minimum wavelength. Results from the application of the hybrid method to multi-mode RMI problems demonstrating the applicability and advantages of the present approach to late-time RMI mixing will be presented in a future paper.

Acknowledgements

Dimitris Drikakis wishes to express his gratitude and appreciation to AWE for their financial support through the William Penney Fellowship award. AWE's financial support with respect to Tommaso Oggian's PhD Case Award is also greatly acknowledged. Tommaso Oggian would also like to thank Dr. Laszlo Konozsy (Cranfield University) for fruitful discussions during the code development. The manuscript contains material ©British Crown Owned Copyright 2014/MoD, reproduced with permission.

References

[1] Volpe, G., 1993. "Performances of compressible flow codes at low Mach number". *AIAA Journal,* **31**, pp. 49–56.

[2] Turkel, E., Fiterman, A., and Van Leer, B., 1994. *Preconditioning and the limit of the compressible to the incompressible flow equations for finite differences schemes*. John Wiley and Sons.

[3] Guillard, H., and Murrone, A., 2004. "On the behavior of upwind schemes in the low mach number limit: II. Godunov type schemes.". *Computers and Fluids,* **33**, pp. 65–675.

[4] Guillard, H., and Viozat, C., 1999. "On the behaviour of upwind schemes in the low Mach number limit". *Computers and Fluids,* **28**, pp. 63–86.

[5] Thornber, B., Drikakis, D., Williams, R., and Youngs, D., 2008a. "On entropy generation and dissipation of kinetic energy in high-resolution shock-capturing schemes". *Journal of Computational Physics,* **227**, pp. 4853–4872.

[6] Thornber, B., Mosedale, A., Drikakis, D., Youngs, D., and Williams, R., 2008b. "An improved reconstruction method for compressible flow with low Mach number features". *Journal of Computational Physics,* **227**, pp. 4873–4894.

[7] Drikakis, D., and Rider, W., 2004. *High resolution methods for incompressible and low-speed flows*. Springer-Verlag, Berlin.

[8] Schnochet, S., 1994. "Fast singular limits of hyperbolic PDEs". *Journal of Differential Equations,* **114**, pp. 476–512.

[9] Grenier, E., 1997. "Oscillatory perturbations of the Navier-Stoke equations". *Journal de Mathmatiques Pures et Appliques,* **76**, pp. 477–498.

[10] Sesterhenn, J., Mller, B., and Thomann, H., 1999. "On the cancellation problem in calculating compressible low Mach number flows". *Journal of Computational Physics,* **151**, pp. 597–615.

[11] Klein, R., 1995. "Semi-implicit extension of a Godunov-type scheme based on low Mach number asymptotics I: One-dimensional flow". *Journal of Computational Physics,* **121**, pp. 213–237.

[12] Roller, S., and Munz, C., 2000. "A low mach number scheme based on multi-scale asymptotics". *Computing and Visualization in Science,* **3**, pp. 85–91.

[13] Schneider, T., Botta, N., Geratz, K., and Klein, R., 1999. "Extension of finite volume compressible flow solvers to multi-dimensional, variable density zero Mach number flows". *Journal of Computational Physics,* **155**, pp. 248–286.

[14] Thornber, B., and Drikakis, D., 2008. "Numerical dissipation of upwind schemes in low Mach flow". *International Journal of numerical Methods sin Fluids,* **56**, pp. 1535–1541.

[15] Eberle, A., 1987. Characteristic flux averaging approach to the solution of Euler's equations. Tech. Rep. Lecture Series 1987-04, Von Karman Institute for Fluid Dynamics.

[16] Drikakis, D., and Tsangaris, S., 1991. "An Implicit Characteristic Flux Averaging Scheme for the Euler Equations for Real Gases". *International Journal of numerical Methods in Fluids,* **12**, pp. 711–726.

[17] Zoltak, J., and Drikakis, D., 1998. "Hybrid upwind methods for the simulation of unsteady shock-wave diffraction over a cylinder". *Computer Methods in Applied Mechanics and Engineering,* **162**, pp. 165–185.

[18] Kim, K. H., and Kim, C., 2005. "Accurate, effcient and monotonic numerical methods for multi-dimensional compressible ows Part II: Multi-dimensional limiting process". *Journal of Computational Physics,* **208**, pp. 570–615.

[19] Rusanov, V. V., 1961. "Calculation of interaction of non-steady shock waves with obstacles". *USSR Computational Mathematics and Mathematical Physics,* **1**, pp. 267–279.

[20] Chorin, A., 1968. "Numerical solution of the Navier-Stokes equations for an incompressible fluid.". *Mathematics of Computation,* **22**, pp. 745–762.

[21] Chorin, A. J., 1969. "On the convergence of discrete approximations to the Navier-Stokes equations". *Mathematics of Computation,* **23**, pp. 341–353.

[22] Chorin, A. J., and Marsden, G., 1993. *A mathematical introduction to fluid-mechanics*. Springer-Verlag, New York.

[23] Van der Vorst, H., 1992. "Bi-CGSTAB: A fast and smoothly converging variant of Bi-CG for the solution of nonsymmetric linear systems". *SIAM Journal on Scientific Computing,* **13**(2), pp. 631–644.

[24] Li, X. L., and Zhang, Q., 1997. "A comparative numerical study of the Richtmyer-Meshkov instability with nonlinear analysis in two and three dimensions". *Physics of Fluids,* **9**(10), pp. 3069–3077.

[25] Melnikov, R., 1995. Numerical anomalies mimicking physical effects. Tech. rep., Los Alamos National Laboratory.

[26] Aleshin, A. N., Gamali, i. E. G., Zaitsev, S. G., Lazareva, E. V., Lebo, I. G., and Rozanov, V. B., 1988. "Nonlinear and transitional stages in the onset of the Richtmyer-Meshkov instability". *Soviet Technical Physics Letters,* **14**, pp. 466–488.

[27] Velikovich, A. L., and Dimonte, G., 1996. "Nonlinear perturbation theory of the incompressible Richtmyer-Meshkov instability". *Phyical Review Letters,* **76**, pp. 3112–3115.

[28] Roache, P., 1998. *Verification and validation in computational science and engineering*. Hermosa Publishers.

List of Figures

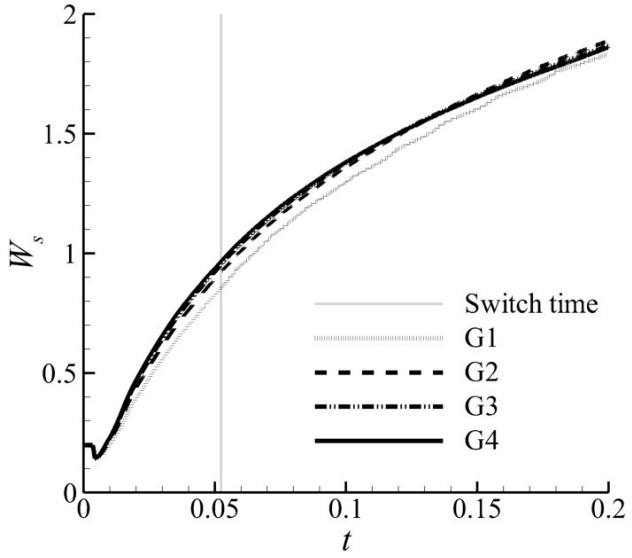

Fig. 1. Grid-convergence for a single-mode instability (H).

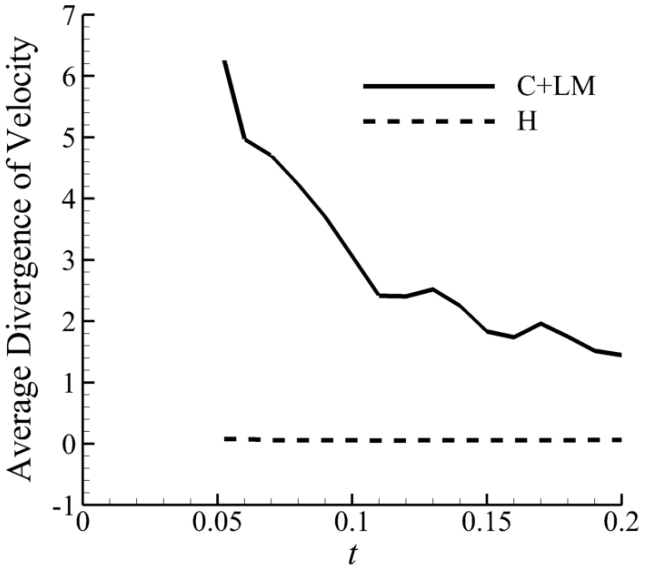

Fig. 2. Absolute average value of velocity divergence at $t > t_{\mathrm{NT}} \approx 0.052$ s for C+LM and H solutions.

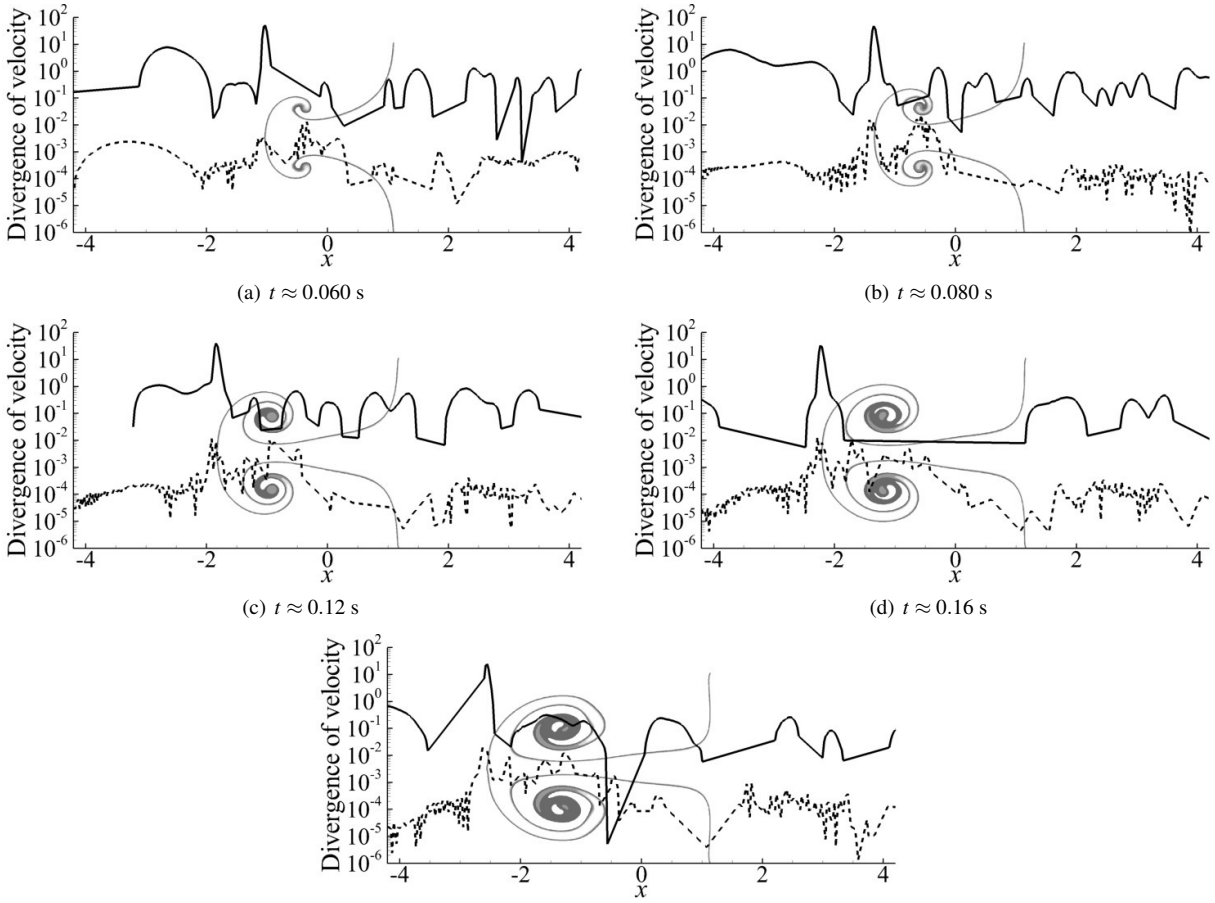

(a) $t \approx 0.060$ s (b) $t \approx 0.080$ s

(c) $t \approx 0.12$ s (d) $t \approx 0.16$ s

(e) $t \approx 0.20$ s

Fig. 3. Divergence of velocity along the central line ($y = \pi$) for C+LM (solid lines) and H (dashed lines) simulations at different time instants $t > t_{\mathrm{NT}}$. The mushroom-like interface between the fluids at each instant is displayed in the background of the graphs.

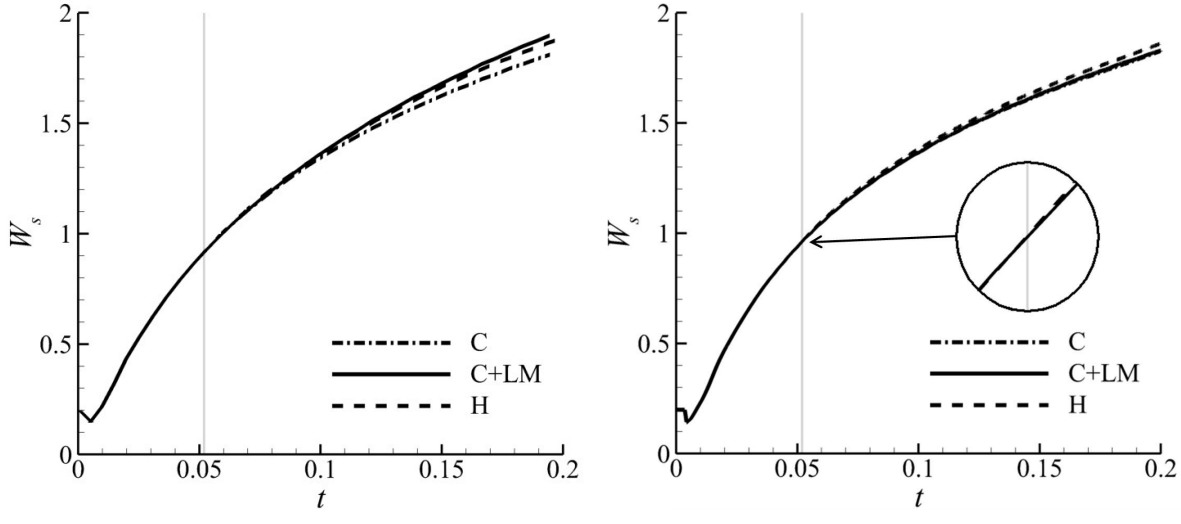

(a) G2 (b) G4

Fig. 4. Predicted growth of the single-mode instability using the compressible (C), compressible with low-Mach correction (C+LM) and hybrid (H) methods.

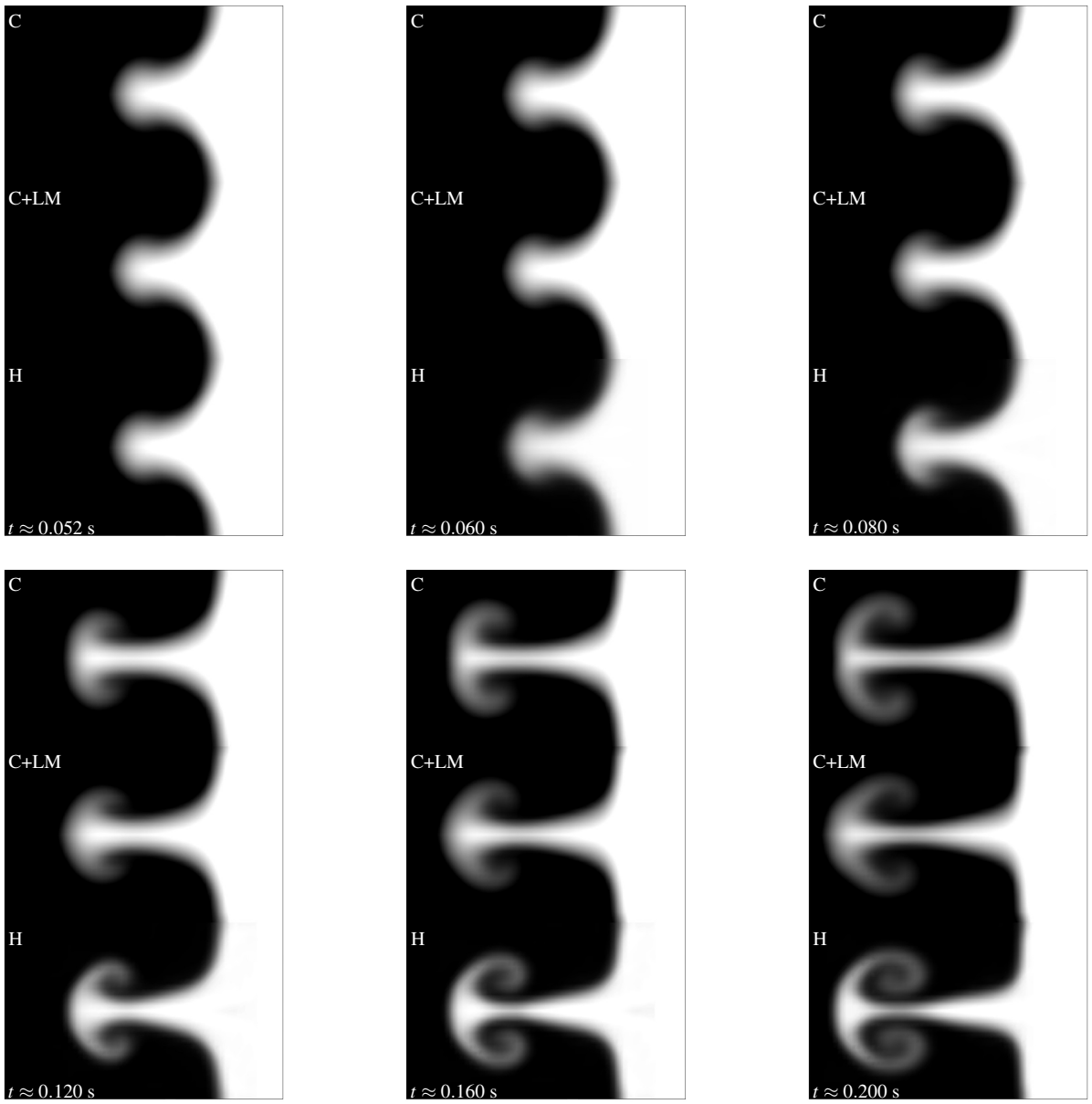

Fig. 5. Comparison of volume-fractions at different time instants for the C, C+LM and H methods on grid G2.

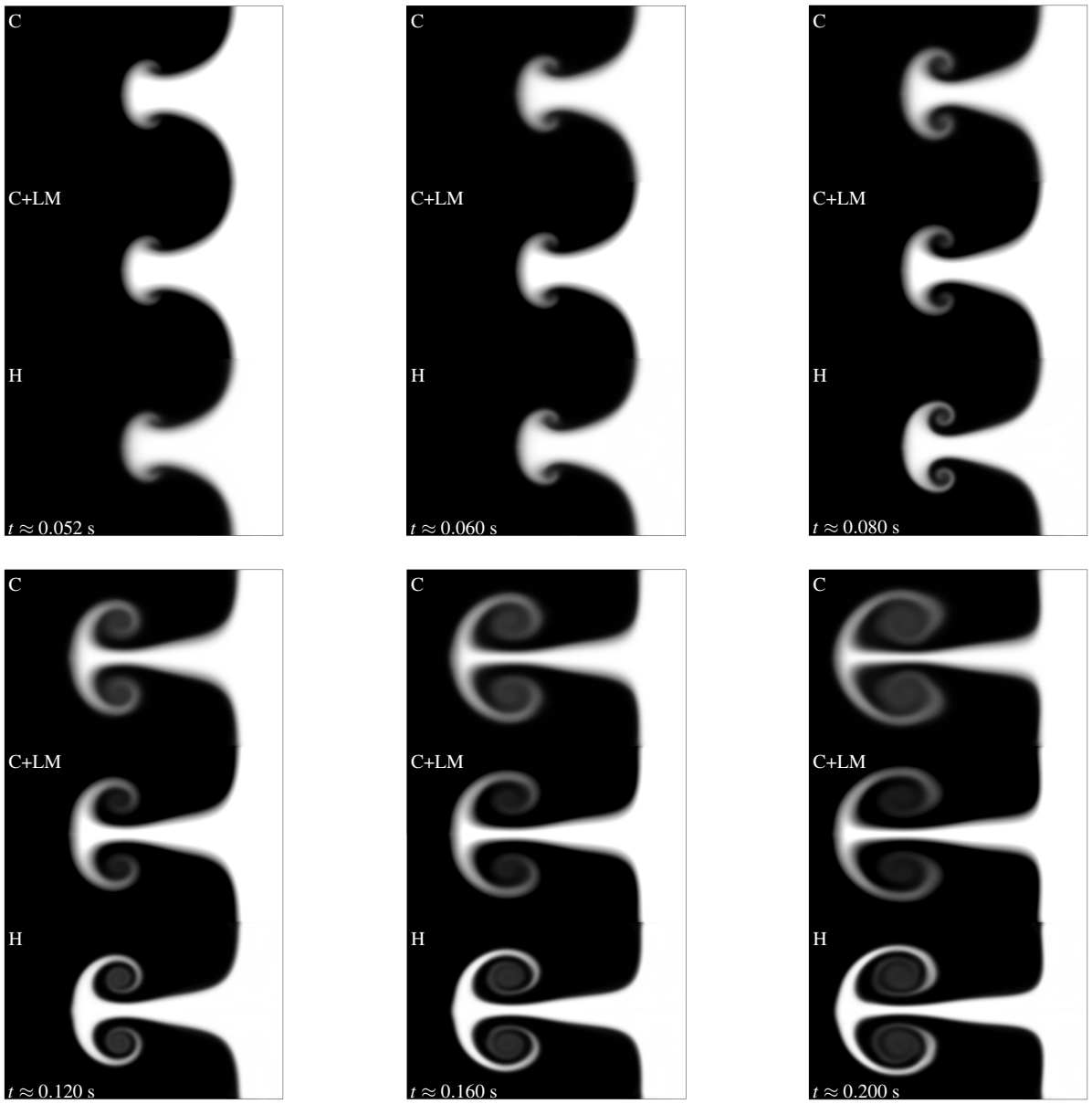

Fig. 6. Comparison of volume-fractions at different time instants for the C, C+LM and H methods on grid G4).